Computational Analysis of Steady State Aerodynamics of Transonic Truss-Braced Wing Configuration in Deep Stall

Juntao Xiong*
KBR Wyle, Inc., Moffett Field, CA 94035, U.S.A.

Nhan Nguyen†
NASA Ames Research Center, Moffett Field, CA, 94035,U.S.A.

John V. Foster‡
NASA Langley Research Center, Hampton, VA 23681, U.S.A.

William E. Milholen§
NASA Langley Research Center, Hampton, VA 23681, U.S.A.

This study presents a computational investigation of steady state aerodynamics of the Subsonic Ultra-Green Aircraft Research (SUGAR) Transonic Truss-Braced Wing (TTBW) configuration over a wide range of angles of attack, from pre-stall to post stall, including conditions associated with deep stall. High-fidelity computational fluid dynamics (CFD) simulations are conducted using FUN3D solver to obtain steady-state aerodynamic solutions. The simulations cover an angle of attack range of $-10°$ to $60°$ and sideslip angles of $0°$ and $15°$, enabling a comprehensive assessment of pre-stall and post-stall aerodynamic behaviors. Reynolds number effect is investigated through comparative analysis of a 4% scale wind-tunnel model and the full scale configuration. Aerodynamic forces and moments are analyzed to assess the effects of Reynolds number and large wind angles on longitudinal and lateral-directional static stability characteristics. Flow field visualizations are employed to examine the progression of flow separation and its influence on aerodynamic characteristics. This study provides valuable insights into the nonlinear aerodynamic and stability characteristics of the SUGAR TTBW configuration at high angles of attack.

I. Introduction

Aircraft stability is one of the important requirements in aircraft design. In particular, ensuring inherently stable flight behaviors without reliance on active control systems is a desirable attribute for both safety and operational robustness. Static stability depends on various design parameters, with the sizing of the horizontal and vertical tails playing a critical role. For longitudinal motion, static stability requires the slope of the pitching moment, referenced to the aircraft's center of gravity (CG), with respect to angle of attack, C_{m_α}, to be negative. This pitching moment results from contributions by both the wing and the horizontal tail, influencing both static and dynamic pitch behaviors. The location of the aircraft's CG is also significant; it is typically positioned slightly ahead of the aerodynamic center based on the mean aerodynamic chord (MAC). The wing lift acting on aerodynamic center generates nose down pitching moment about CG. As the angle of attack increases, the aerodynamic behaviors become increasingly nonlinear due to flow separation. In swept-wing configurations, stall typically initiates near the wingtips and progressively moves inboard with further increases in the angle of attack. The loss of lift at the outboard wing sections reduces the wing's nose down pitching moment contribution, diminishing its counteracting effect on the tail's pitching moment and potentially leading to a pitch break which causes static stability derivative C_{m_α} becoming zero. Beyond this point, a nose-up pitching moment may dominate, creating a static pitch instability. If uncorrected by control surfaces, this can result in a deep stall condition, in which the aircraft enters a high-angle-of-attack regime with reduced recoverability. The

*Aerospace Engineer, Intelligent System Division, juntao.xiong@nasa.gov, Member AIAA.
†Senior Research Scientist and Technical Group Lead, Intelligent Systems Division, MS269; nhan.t.nguyen@nasa.gov. Associate Fellow AIAA.
‡Senior Research Engineer, Flight Dynamic Branch, MS 308, john.v.foster@nasa.gov, Associate Fellow AIAA
§Configuration Aerodynamics Branch, MS 499, william.e.milholen@nasa.gov, Senior Member AIAA

Subsonic Ultra-Green Aircraft Research (SUGAR) Transonic Truss-Braced Wing[1,2,3,4] (TTBW) as shown in Fig. 1 is an advanced aircraft configuration under development, intended to enhance aerodynamic efficiency and reduce fuel consumption for future commercial transport. Characterized by a large aspect ratio high wing supported by struts and a T-tail arrangement, the TTBW configuration may contribute additional unique aerodynamic challenges at high angles of attack.

To address these challenges, a low speed experimental investigation was conducted to examine the high angle of attack aerodynamics of a 4% scale SUGAR TTBW wind tunnel model at NASA Langley Research Center 12-Foot Low-Speed Tunnel (12-Foot LST) under NASA Aeronautics Research Mission Directorate (ARMD) Advanced Air Transport Technologies (AATT) project. Three test entries were completed. This investigation was designed to be a risk reduction effort to support subsequent high-speed, larger scale testing testing in the NASA Langley Research Center 14-by 22-Foot Subsonic Tunnel. In addition, under a joint NASA-Boeing collaboration funded by the AATT project via SUGAR Phase VI-A contract, a 11.8% scale SUGAR TTBW model will be tested at the QinetiQ 5m wind tunnel in the United Kingdom to investigate high-lift performance, stability characteristics, and icing at high Reynolds number.[5] The test will also acquire detailed stability characteristics and evaluate aerodynamic modification using stability enhancement devices including ventral fins, strut flaps, dorsal fins, etc. to improve lateral-directional characteristics.[5]

In parallel, a computational study is performed to support the wind tunnel tests. This paper presents a computational investigation of SUGAR TTBW configuration aerodynamics in deep stall flight conditions. High-fidelity simulations are conducted using FUN3D solver to obtain steady-state aerodynamic solutions over an angle of attack range from -10° to 60° at low speed, and sideslip angles of 0° and 15° to assess both aerodynamic and stability characteristics. Due to the low Reynolds number limitations in the 12-Foot LST, data corrections must be considered to provide any conclusions regarding full scale characteristics. To examine the influence of Reynolds number on aerodynamic performance, both a 4% scale model and a full scale configuration are analyzed using CFD. This approach enables a direct comparison of aerodynamic characteristics across different scales and provides insight into the Reynolds number effect on the SUGAR TTBW configuration.

Figure 1 Boeing SUGAR Transonic Truss-Braced Wing (TTBW) Aircraft Concept.

II. Computational Approach

A. Numerical Code

The computational fluid dynamics code used in this study is FUN3D,[6,7] which solves the unsteady three-dimensional Navier-Stokes equations on mixed-element grids using a vertices-centered finite-volume method. Information exchange for flow computation on different partitions using multiple CPUs is implemented through the MPI (Message Passing Interface) protocol. It employs an implicit upwind algorithm in which the inviscid fluxes are obtained with a flux-difference-splitting scheme. At interfaces delimiting neighboring control volumes, the inviscid fluxes are computed

using an approximate Riemann solver based on the values on either side of the interface. The Roe flux difference splitting[8] is used in the current study. For second-order accuracy, interface values are obtained by extrapolation of the control volume centroidal values, based on gradients computed at the mesh vertices, using an unweighted least squares technique. The Venkatakrishnan[9] limiter is used in the current study to limit the reconstructed values when necessary. In this study the tetrahedral mesh with prism layers are used. In FUN3D, for tetrahedral meshes, the full viscous fluxes are discretized using a finite-volume formulation in which the required velocity gradients on the dual faces are computed using the Green-Gauss theorem. The solution at each time-step is updated with a backwards Euler time-differencing scheme. At each time step, the system of equations is approximately solved with either a multi-color point-implicit procedure or an implicit-line relaxation scheme. Local time-step scaling is employed to accelerate convergence to steady-state. To model turbulent flows, the one-equation model of Spalart-Allmaras[10] (S-A) is used in this study.

B. Computational Model and Grid

The geometry used in the CFD analysis is the SUGAR TTBW configuration. In this study, the wind tunnel walls and wind tunnel model support geometry are not included in the CFD model. The TTBW configuration geometry is illustrated in Fig. 2, where $\bar{c}$ denotes the wing mean aerodynamic chord length. The balance center, indicated by the pink dot in Fig. 2, is located at the 25% of the wing mean aerodynamic chord. All moments calculations are referenced to the balance center of the wind tunnel model. Figure 3 shows the surface mesh of the geometry. The volume mesh is comprised of tetrahedral elements and a prism layer near the wall. The prism layer is used to resolve the turbulent boundary layer. The $y+$ of the first cell from the wall is less than 1. The mesh contains approximately 120 million nodes.

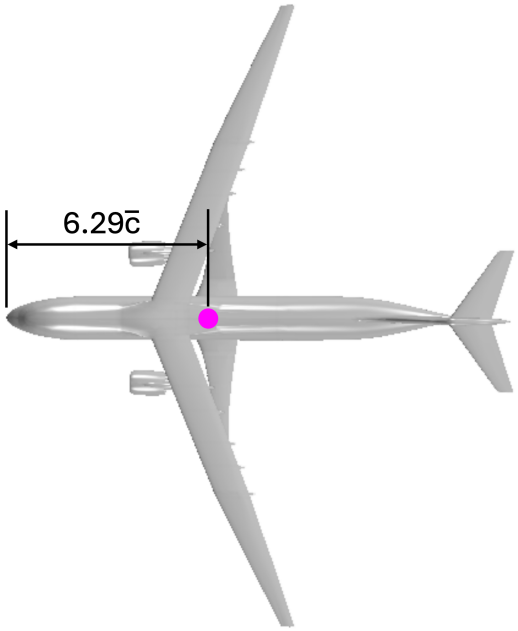

(a) Top View

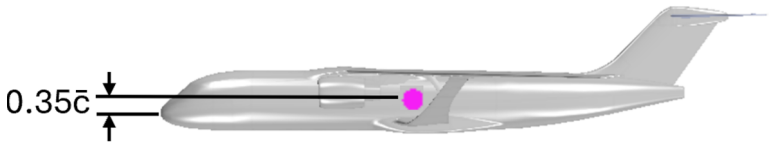

(b) Side View

Figure 2 TTBW Geometry.

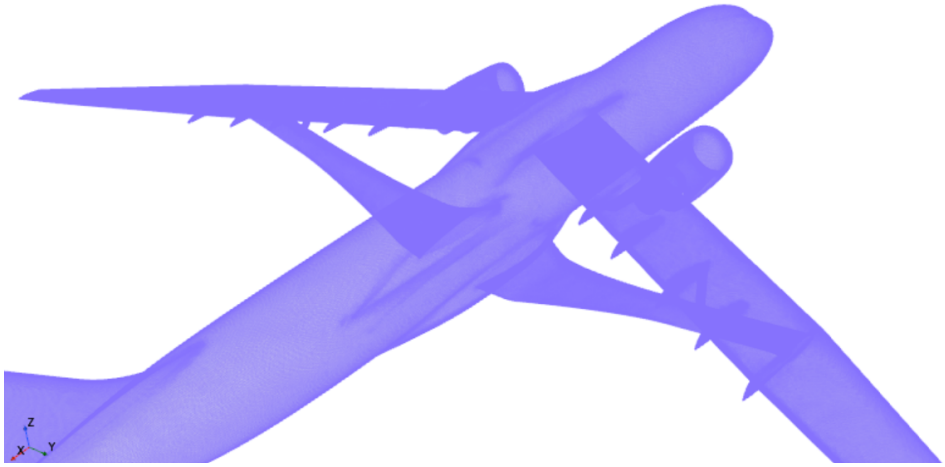

Figure 3 TTBW Geometry CFD Mesh.

C. Low-speed preconditioning

The 12-Foot LST test dynamic pressure is about 4 psf, which corresponds to a Mach number of 0.052. To perform CFD simulations at this low Mach number, a low-speed preconditioning is required to improve the accuracy and convergence. Turkel's[6] low-speed preconditioning is used in this study. Figure 4 shows the x-momentum time history convergence with and without the low-speed preconditioning at Mach 0.052 and zero angle of attack. Without the low-speed preconditioning, it takes 30,000 iterations for the residual reach 10^{-6}. With the preconditioning, the same level of residual is achieved in only about 3,000 iterations. Figure 5 shows the lift time history convergence. The lift converges more rapidly to a higher value when the low-speed preconditioning is applied. Figure 6 presents the pressure coefficient distribution at wing station $\eta = 73\%$. The pressure profile is noticeably smoother with the low-speed preconditioning. In contrast, the solution without the low-speed preconditioning exhibits non-physical oscillations near the leading edge and trailing edge, resulting larger pressure spikes, particularly at the trailing edge.

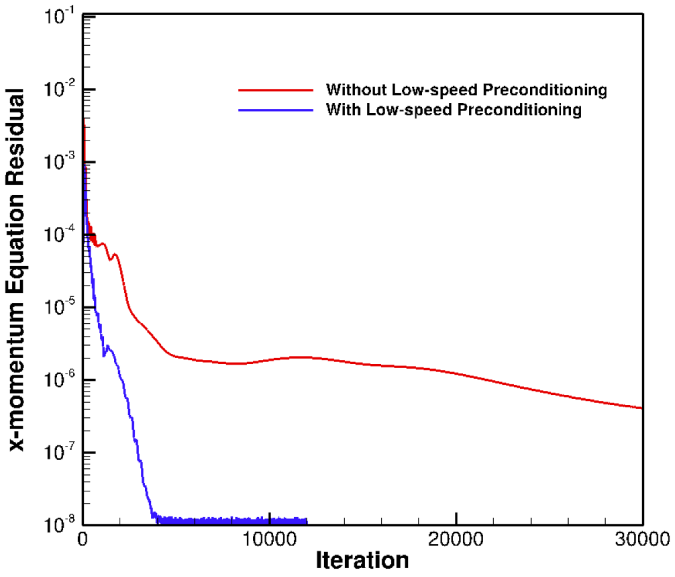

Figure 4 Comparison of x-momentum Time History Convergence at Mach 0.052 and Angle of Attack 0°.

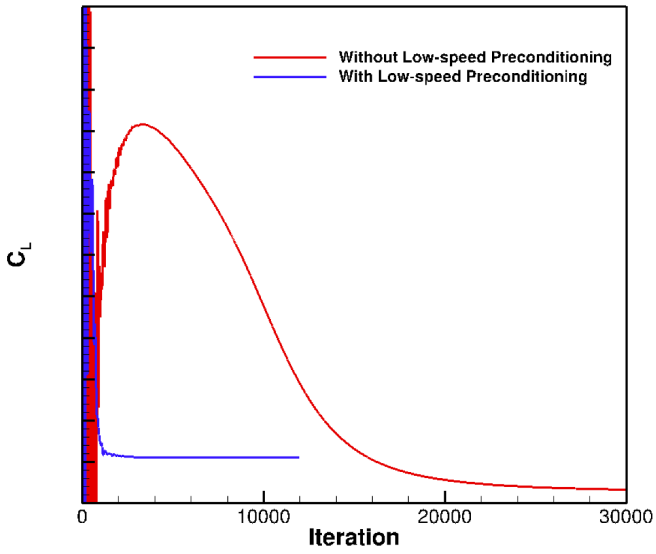

Figure 5 Comparison of Lift Time History Convergence at Mach 0.052 and Angle of Attack 0°.

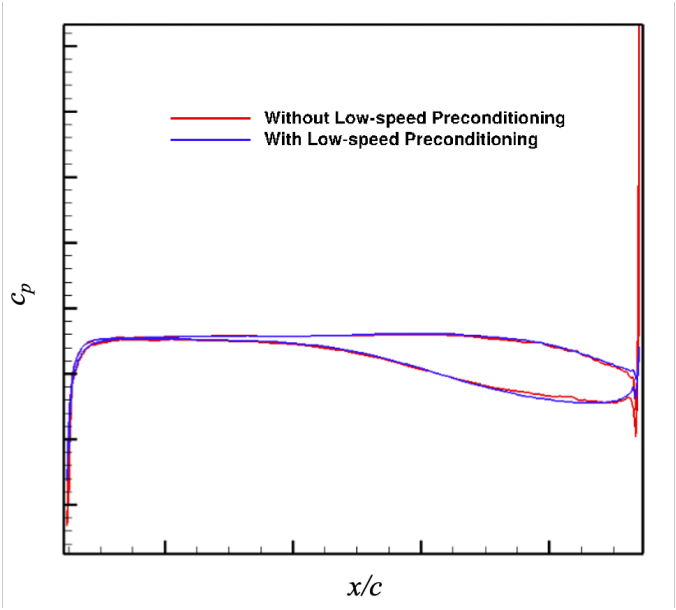

Figure 6 Comparison of Pressure Coefficient Profiles at Wing Station η = 73% at Mach 0.052 and Angle of Attack 0°.

III. Computational Results

A. Steady-state Simulations

As previously stated, the 12-Foot LST test dynamic pressure is about 4 psf, which corresponds to a Mach number of 0.052. The URANS simulations are first performed for the 4% scale SUGAR TTBW configuration at Mach number 0.052 over angles of attack range from $-10°$ to 60°, and sideslip angles 0° and 15°. The simulation results are then compared with the wind tunnel measurements. The comparison shows that the longitudinal aerodynamic coefficients

C_L, C_D, C_m and the lateral-directional aerodynamic coefficients C_Y, C_l, C_n at 15° sideslip are in good agreement with the test data. The full experimental data report will be published in the future.

The good agreement between the CFD predictions and the available measurements provides confidence in the validity of the CFD model. Subsequently, the full scale configuration is simulated at Mach 0.2 to examine the Reynolds number effect on aerodynamic characteristics at high angles of attack. At Mach 0.2, the flow remains in the low speed regime, and the compressibility effect is generally negligible. The following figures are presented without values shown on the axes due to data restrictions.

Figure 7 shows the time-averaged lift coefficients for both the 4% scale and full scale TTBW configurations under sideslip angles of 0° and 15°. The lift coefficients are similar for sideslip angles of 0° and 15° for both scales. At angle of attack from 0° to 8°, the lift curves for both scales exhibit nearly linear behavior, with minimal influence from the Reynolds number or sideslip angle. Figure 7 (a) shows that the nonlinear behaviors occur when the angle of attack exceeds 8° for the 4% scale model. Figure 7 (b) shows that the linear portion of the lift coefficient curve for the full scale configuration persists to angle of attack up to 10° and attains higher lift coefficient values, indicating the Reynolds number effect on lift coefficient due to the delayed flow separation. The maximum lift coefficient for the full scale case occurs near angle of attack 15°, followed by a gradual reduction with further increase in angle of attack. The 4% scale model exhibits an earlier stall onset when comparing $C_{L_{max}}$ with the full scale configuration at 15° angle of attack, reflecting the lower Reynolds number effect on flow separation behavior in the sub-scale model. At angles of attack above 30°, the lift coefficient trends for both 4% scale and full scale converge. The flow is fully separated for both configurations, and the resulting separation dominated behavior diminishes the influence of Reynolds number effect.

Figure 8 shows the time-averaged drag coefficients. The drag coefficient increases almost linearly when the angle of attack exceeds 8°. The full scale configuration shows lower drag at angles of attack under 30° due to its thinner boundary layer.

The time-averaged pitching moment coefficients for both the 4% scale and full scale TTBW configurations are presented in Fig. 9. For the 4% scale model (Fig. 9 (a)), the first and second pitch breaks occur at angles of attack 8° and 16° respectively, for both sideslip angles. In contrast, the full scale configuration (Fig. 9 (b)) exhibits its first pitch break at angle of attack 10° and the second at angle of attack 16°. This shift in the initial pitch break angle indicates that the higher Reynolds number delays flow separation, thereby postponing the onset of the pitch break.

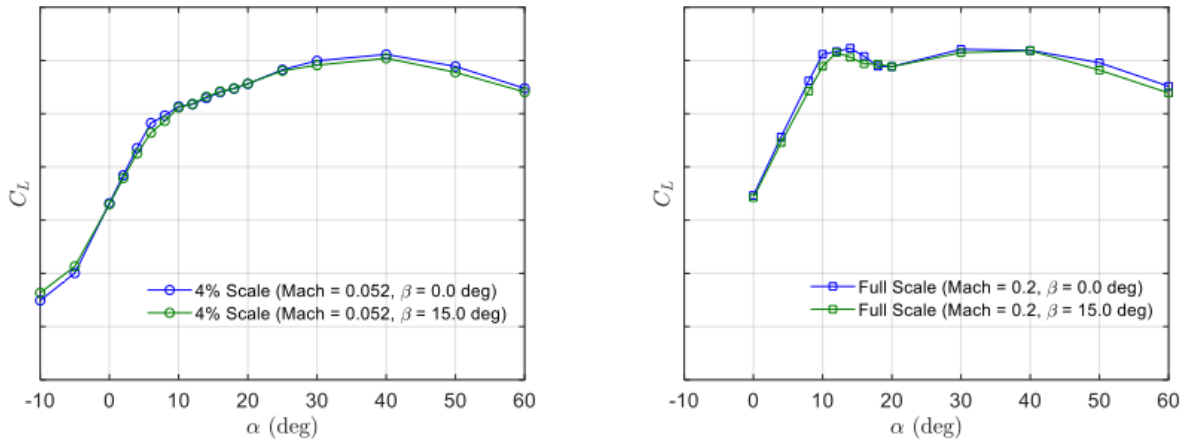

(a) 4% Scale

(b) Full Scale

Figure 7 Lift Coefficients of TTBW.

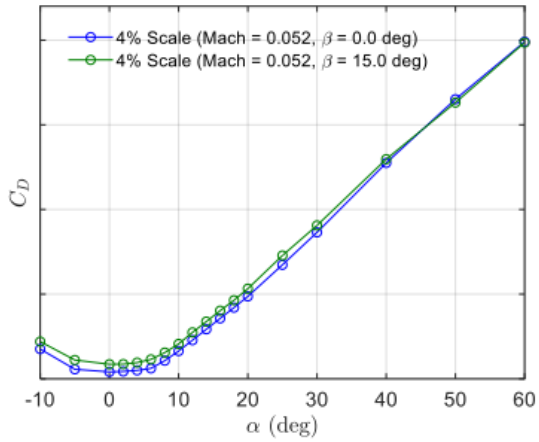

(a) 4% Scale

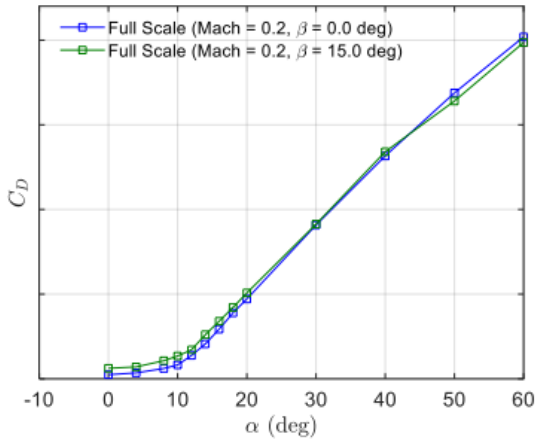

(b) Full Scale

Figure 8 Drag Coefficients of TTBW.

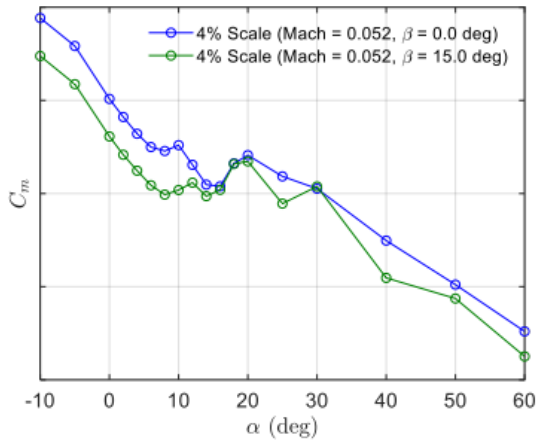

(a) 4% Scale

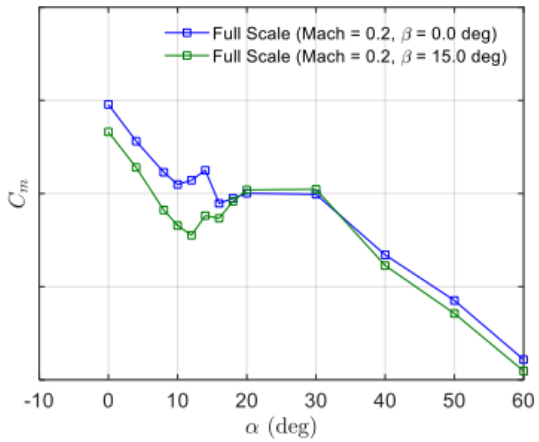

(b) Full Scale

Figure 9 Pitching Moment Coefficients of TTBW.

The lift and pitching moment contributions from the wing alone without the struts and horizontal tail for both the 4% scale and full scale TTBW configurations are shown in Fig. 10 - Fig. 13. For the 4% scale model (Fig. 10 (a) and Fig. 12 (a)), at an angle of attack 8°, flow separation occurs on the wing, inducing nonlinearity in the lift coefficient and pitching moment coefficient, which leads the first pitch break in the TTBW configuration. At an angle of attack 16° which are shown in Fig. 11 (a) and Fig. 13 (a), stall of the horizontal tail results in nonlinearity in lift coefficient and pitching moment coefficient, corresponding to the second pitch break of the TTBW configuration. For the full scale configuration (Fig. 10 (b) and Fig. 12 (b)), flow separation occurs on the wing at an angle of attack 10°, which leads the first pitch break of the model. The Fig. 11 (b) and Fig. 13 (b) show that the nonlinear behaviors occur on the horizontal tail when the angle of attack exceeds 12°, the stall of the horizontal tail results in second pitch break.

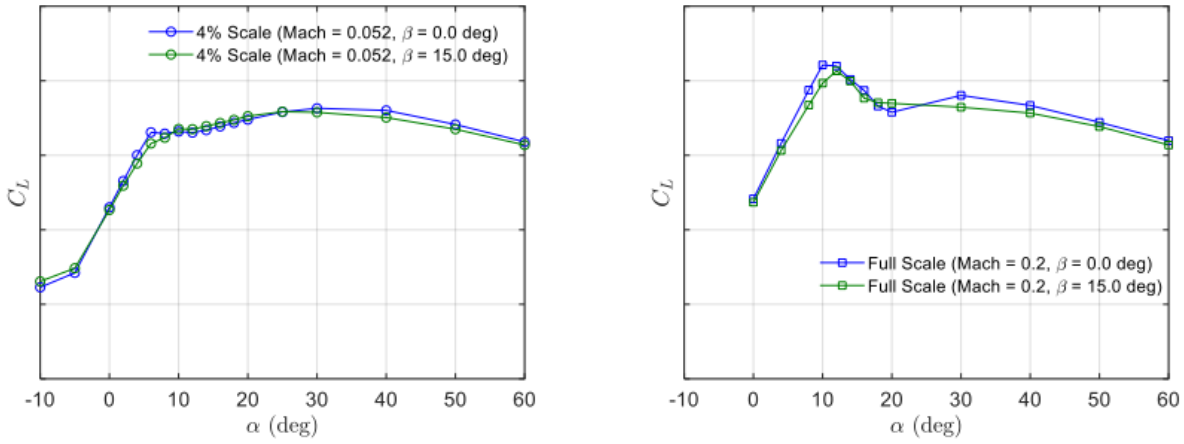

(a) 4% Scale (b) Full Scale

Figure 10 Lift Coefficients of TTBW Wing Component.

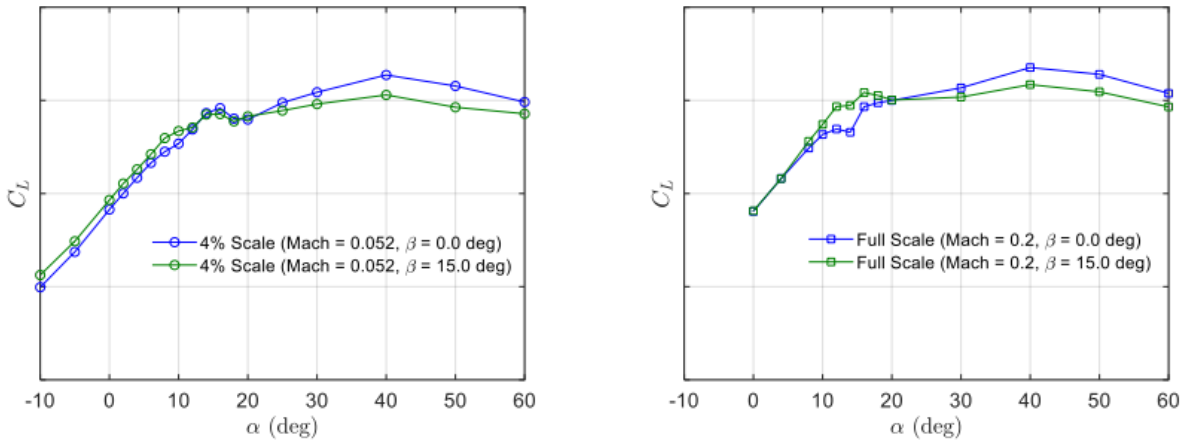

(a) 4% Scale (b) Full Scale

Figure 11 Lift Coefficients of TTBW Horizontal Tail Component.

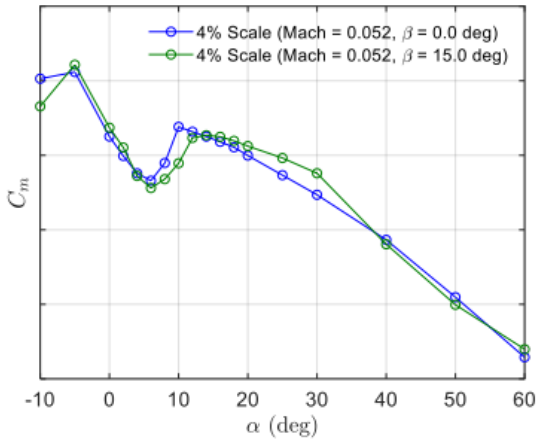

(a) 4% Scale

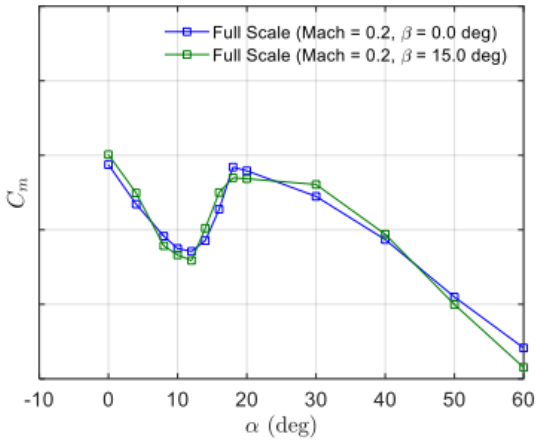

(b) Full Scale

Figure 12 Pitching Moment Coefficients of TTBW Wing Component.

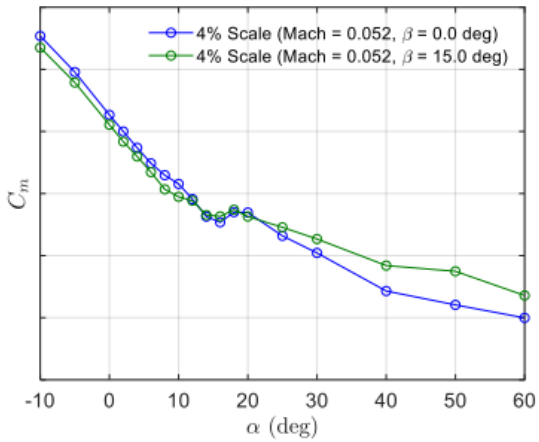

(a) 4% Scale

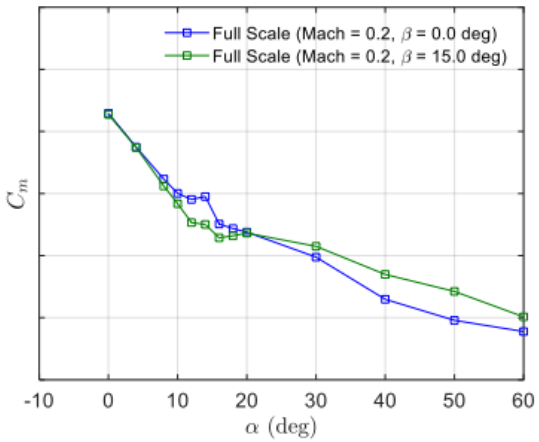

(b) Full Scale

Figure 13 Pitching Moment Coefficients of TTBW Horizontal Tail Component.

Figure 14 presents the time-averaged side force coefficients for both the 4% scale and full scale TTBW configurations at sideslip angle of 15°. The side force coefficients are negative throughout the angle of attack range.

Figure 15 shows the time-averaged rolling moment coefficients for both the 4% scale and full scale TTBW configurations. At a sideslip angle of 15°, the rolling moment coefficients are negative for angles of attack greater than −10° for the 4% scale model. The negative rolling moment coefficients imply static roll stability under positive sideslip condition. For the full scale configuration, the rolling moment coefficients become more negative between angles of attack of 10° to 30°.

Figure 16 displays the time-averaged yawing moment coefficients for both the 4% scale and full scale TTBW configurations. The yawing moment coefficients for 4% scale model become negative between the angles of attack of 8° to 23°, and again beyond 45°, indicating static yaw instability at these ranges under positive sideslip condition. For the full scale configuration, the onset of negative yawing moment coefficient is delayed to angle of attack 12°. This behavior suggests that the higher Reynolds number effect delays the flow separation, thereby postponing the onset of the static yaw instability.

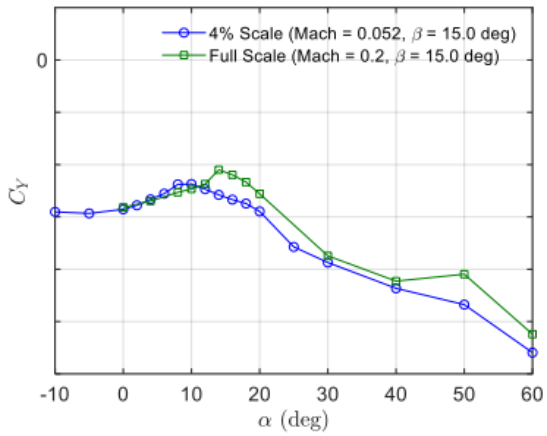

Figure 14 Side Force Coefficients of TTBW.

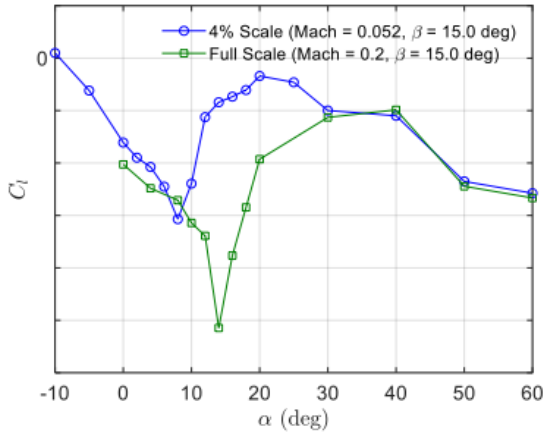

Figure 15 Rolling Moment Coefficients of TTBW.

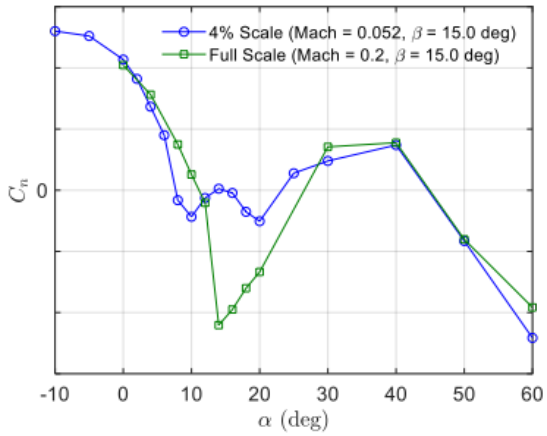

Figure 16 Yawing Moment Coefficients of TTBW.

Figures 17 - 20 present surface pressure contour and streamline plots for the 4% scale and full scale TTBW configurations at angles of attack 16° and 60°, and sideslip angles of 0° and 15°. The negative pressure coefficient regions are shown in blue, indicating suction, while positive regions are colored in red.

For the 4% scale model, at an angle of attack 16°, as shown in Fig 17 (a), flow separation is observed near the wing root and the nacelle region. Additionally, a pressure suction is present at the leading edge of the horizontal tail. For the full scale configuration, at an angle of attack 16°, as shown in Fig 18 (a), separation regions near the wing root and the nacelle are smaller and several leading edge suction pockets are observed in the outboard wing region. With a sideslip angle of 15°, shown in Fig 17 (b) and Fig 18 (b), separation intensifies over the left wing and strut. The sideslip also induces higher pressure on the right surface of the vertical tail. At a high angle of attack of 60° for both scales, Fig 19(a) and Fig 20(a) illustrate widespread flow separation over the wing, strut, and fuselage. Slight flow asymmetry is also observed event at zero sideslip, likely due to unsteady vortex behaviors. With a sideslip angle of 15° for both scales, as shown in Fig 19 (b) and Fig 20 (b), a pronounced low pressure region forms near the right wingtip. On the right surface of the vertical tail exhibits a region of positive pressure.

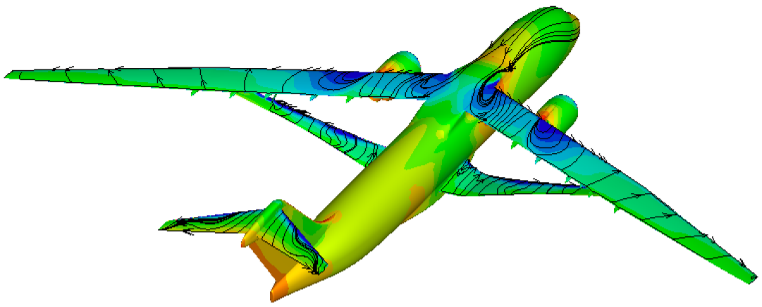

(a) $\beta = 0°$

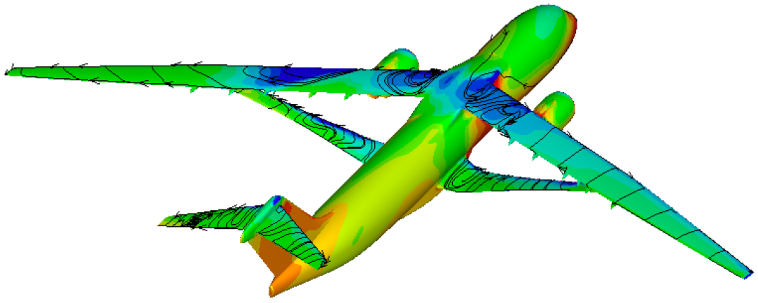

(b) $\beta = 15°$

Figure 17 Pressure Coefficient Contour on 4% Scale TTBW at Mach 0.052 and Angle of Attack 16°.

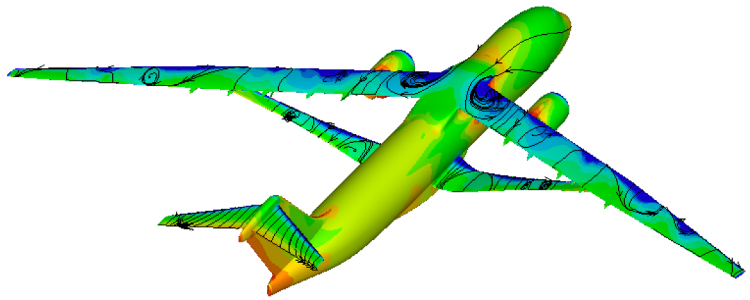

(a) $\beta = 0°$

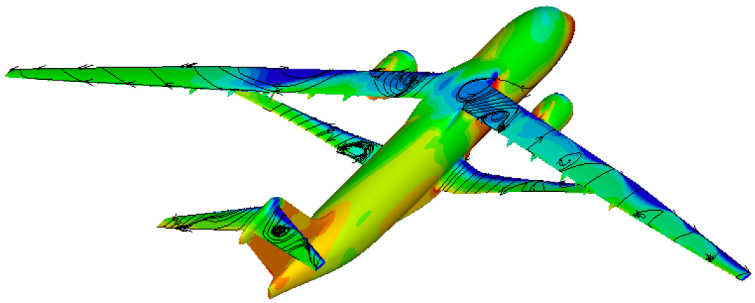

(b) $\beta = 15°$

Figure 18 Pressure Coefficient Contour on Full Scale TTBW at Mach 0.2 and Angle of Attack 16°.

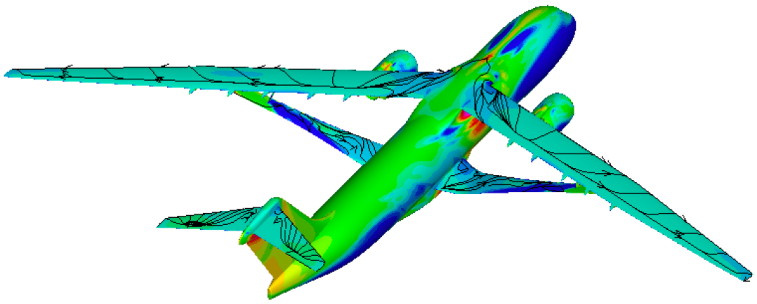

(a) $\beta = 0°$

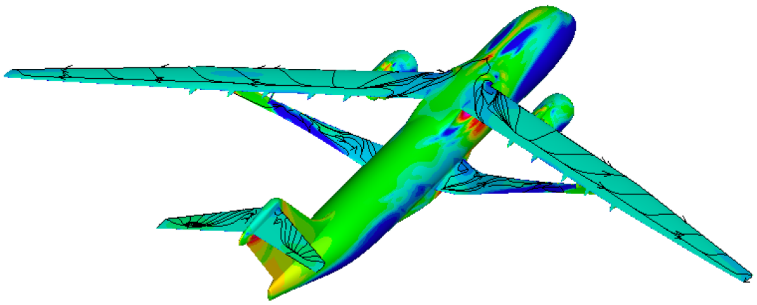

(b) $\beta = 15°$

Figure 19 Pressure Coefficient Contour on 4% Scale TTBW at Mach 0.052 and Angle of Attack 60°.

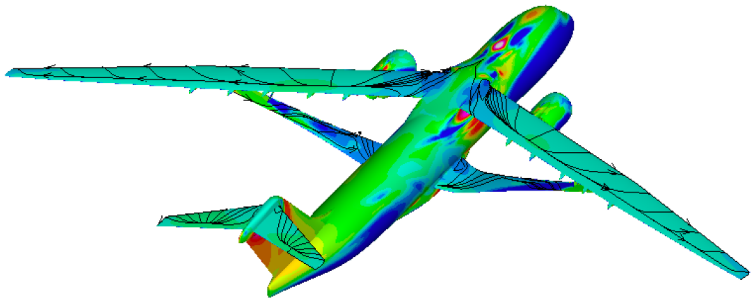

(a) $\beta = 0°$

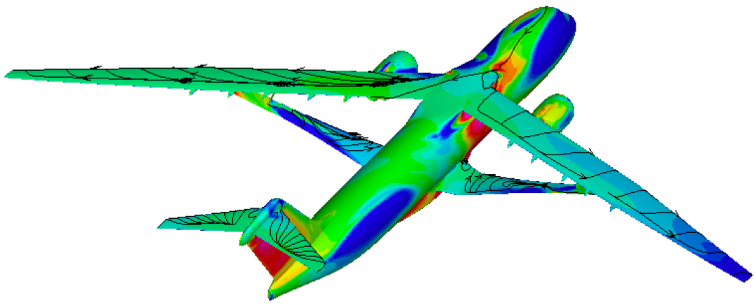

(b) $\beta = 15°$

Figure 20 Pressure Coefficient Contour on Full Scale TTBW at Mach 0.2 and Angle of Attack 60°.

Figures 21 - 24 present vorticity magnitude contours for the 4% scale and full scale TTBW configurations at angles of attack 16° and 60°, and sideslip angles of 0° and 15°.

Figure 21 show the 4% scale results at angle of attack 16°. A coherent vortex originates along the upper surface near the forward portion of the fuselage and convects downstream. When a 15° sideslip is introduced, this structure becomes asymmetric, producing a pair of vortices that impinge directly on the vertical tail. The corresponding full-scale contours are show in Fig. 22. At the higher Reynolds number, the vortical structure remains similar in topology but becomes slightly smaller and weaker in intensity, consistent with delayed separation and a more energized boundary layer. This explains the larger static yaw stability margin for the full scale configuration.

Figures 23 and 24 show the results at angle of attack 60° for both scales. At this extreme condition, the flow is fully separated, and the vortex system is dominated by large, separated structures. At 15° sideslip angle, a strong asymmetric pair of vortices forms and propagates downstream toward the vertical tail. These vortices impinge on the empennage and are likely to degrade directional stability and control effectiveness.

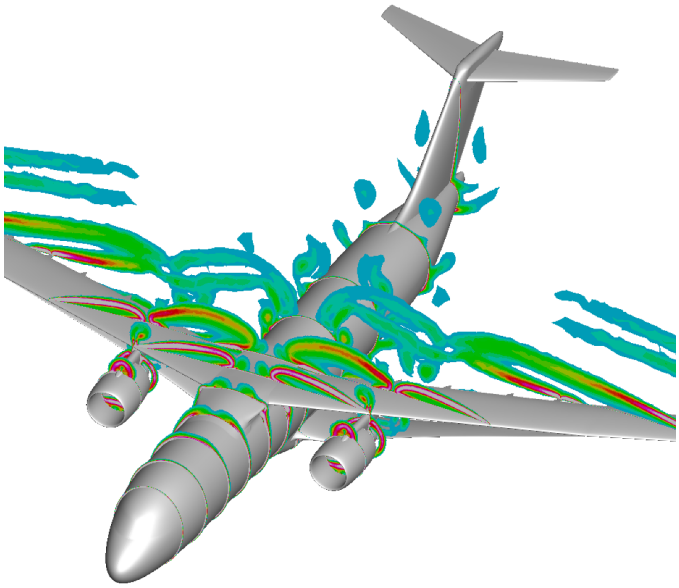

(a) $\beta = 0°$

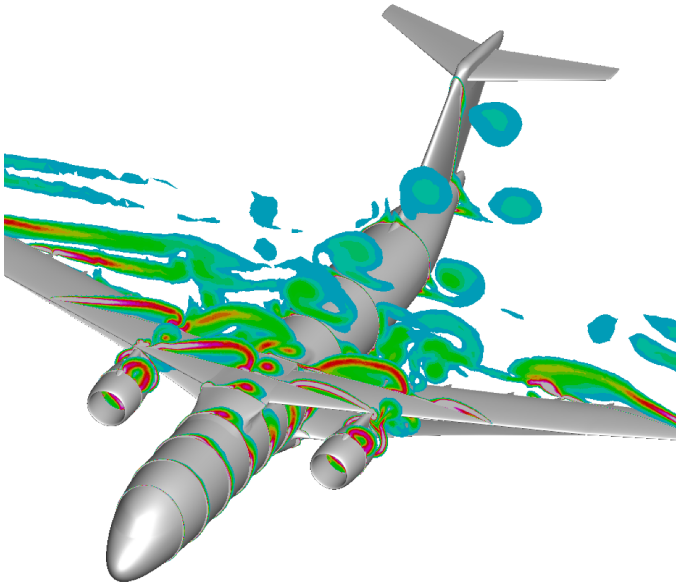

(b) $\beta = 15°$

Figure 21 Vorticity Magnitude Contour on 4% Scale TTBW at Mach 0.052 and Angle of Attack 16°.

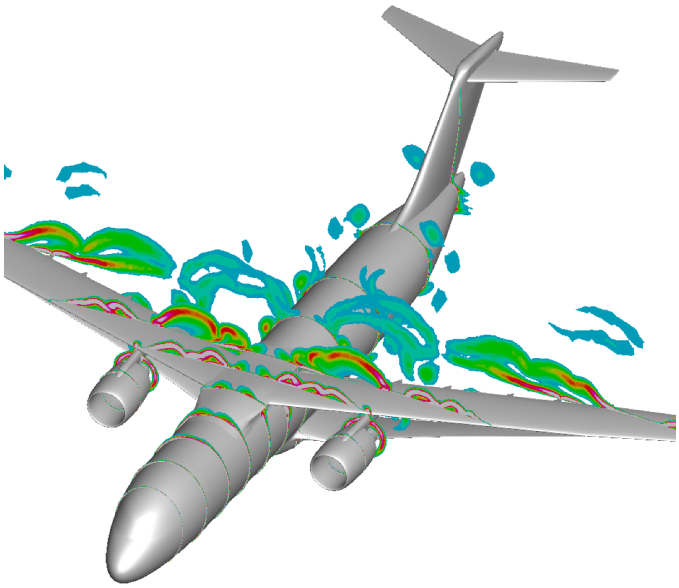

(a) $\beta = 0°$

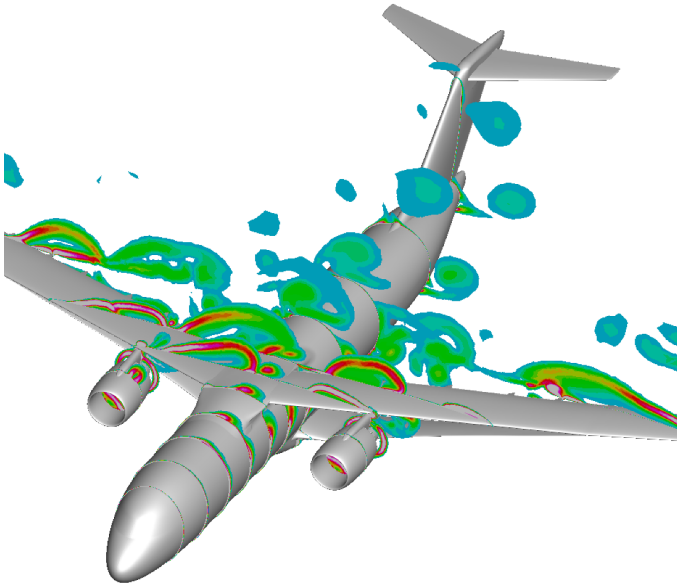

(b) $\beta = 15°$

Figure 22 Vorticity Magnitude Contour on Full Scale TTBW at Mach 0.2 and Angle of Attack 16°.

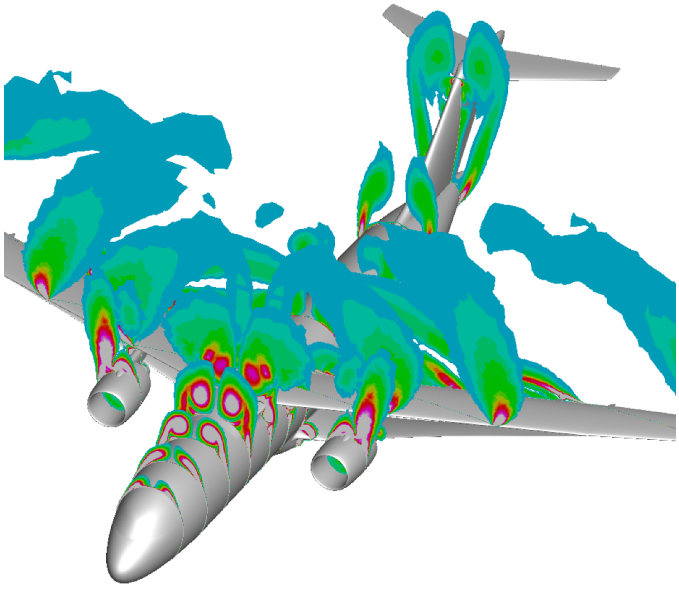

(a) $\beta = 0°$

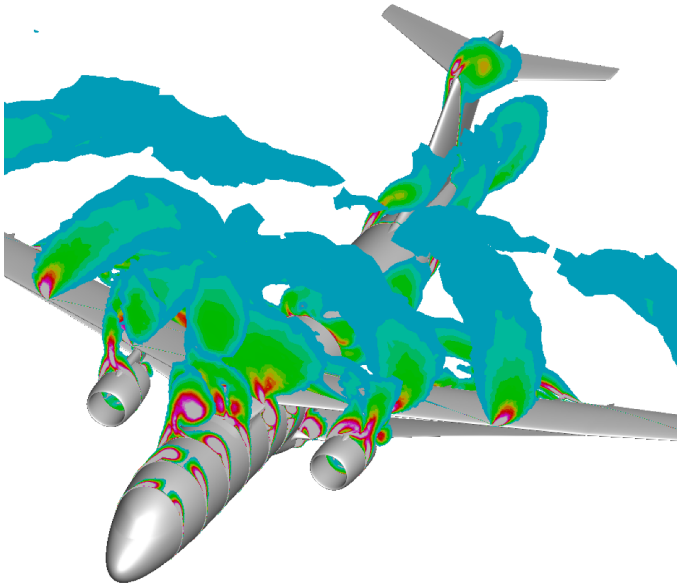

(b) $\beta = 15°$

Figure 23 Vorticity Magnitude Contour on 4% Scale TTBW at Mach 0.052 and Angle of Attack 60°.

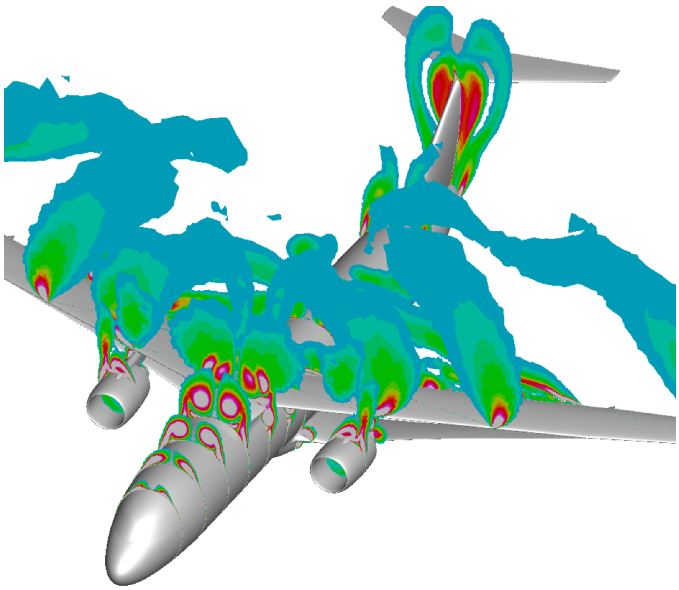

(a) $\beta = 0°$

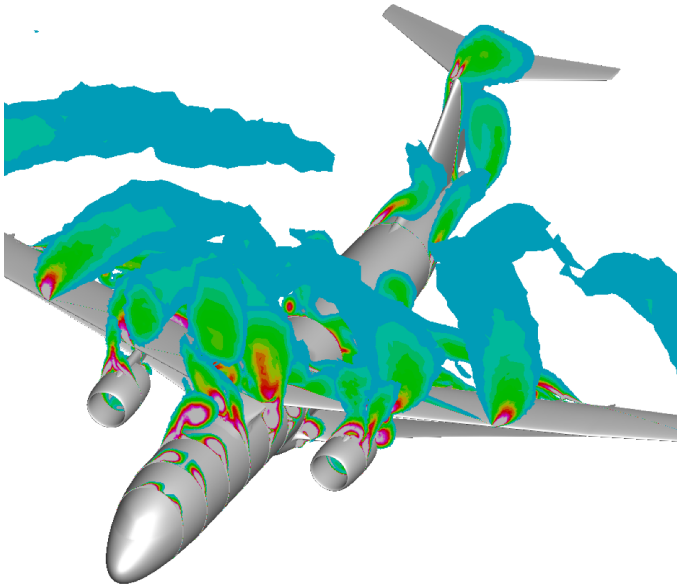

(b) $\beta = 15°$

Figure 24 Vorticity Magnitude Contour on Full Scale TTBW at Mach 0.2 and Angle of Attack 60°.

Figures 25 - 40 present pressure contour and streamline plots in two-dimensional x-z and x-y planes, illustrating flow behaviors over TTBW at various angles of attack and sideslip angles. In the two-dimensional plane plots, a notional NACA airfoil profile is included to illustrate the cross sections.

Figure 25 shows x-z plane cuts at an angle of attack of 16° and sideslip angle 0° for the 4% scale model, taken at the left and right wing station $\eta = 9\%$, corresponding to the horizontal tail MAC station. Flow separation is clearly observed near the wing and strut root region. The separated flow impinges on the horizontal tail, reducing its aerodynamic effectiveness and contributing to pitch instability. Figure 27 presents the x-y plane cut at vertical tail MAC station, highlighting the spanwise flow development. The flow is symmetric at the angle of attack of 0°. For the full scale configuration pressure contours in Fig. 26 and Fig.28, the qualitative features at angle of attack of 16° and sideslip angle 0° are similar; however, the extent of separated flow is reduced. The higher Reynolds number promotes a thinner,

more energized boundary layer, delaying flow detachment over the wing surfaces. As a result, the separated regions are smaller and weaker than in the 4% scale model.

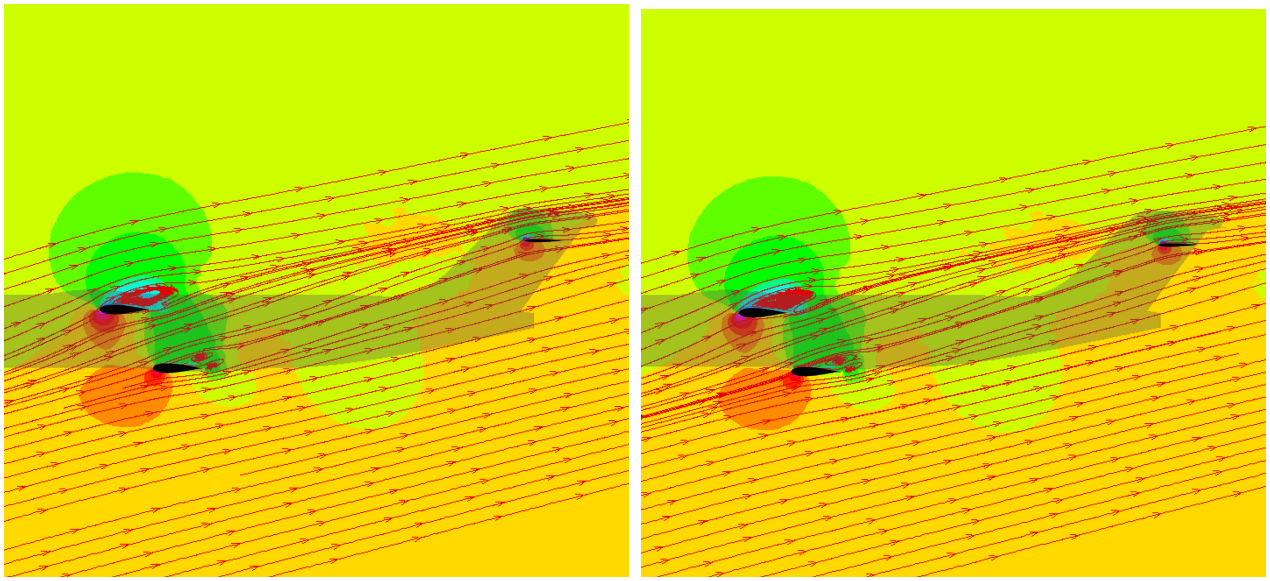

(a) $\eta = -9\%$ (b) $\eta = 9\%$

Figure 25 4% Scale TTBW Flow Field in x-z Plane (Notional NACA Airfoil Shown) at Mach 0.052, Angle of Attack 16°, and Sideslip Angle 0°.

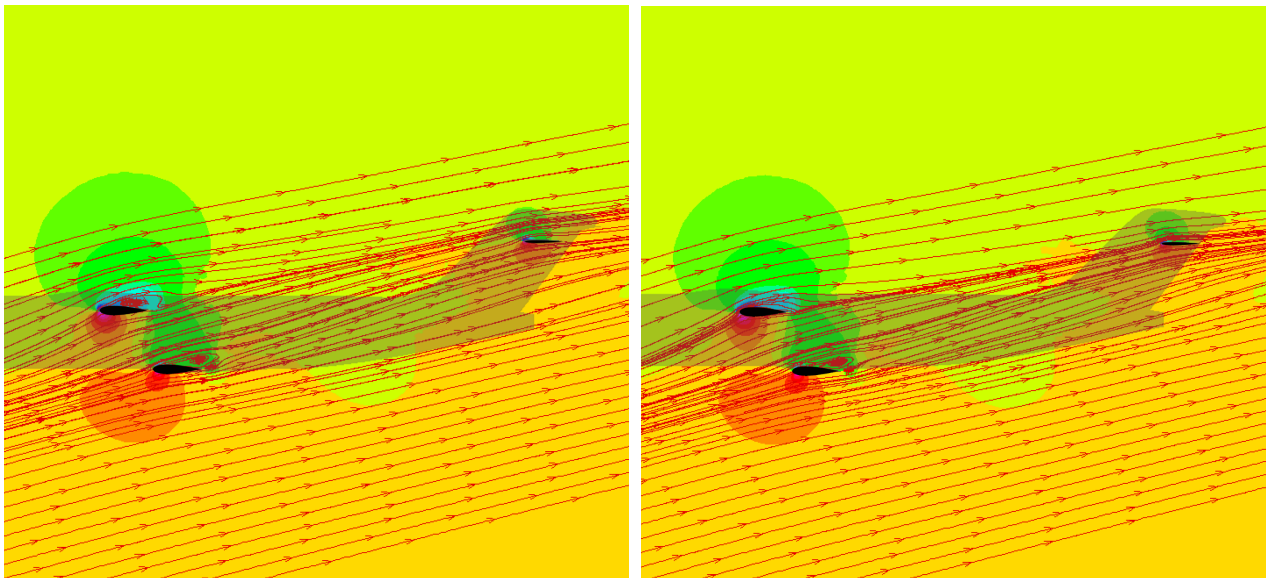

(a) $\eta = -9\%$ (b) $\eta = 9\%$

Figure 26 Full Scale TTBW Flow Field in x-z Plane (Notional NACA Airfoil Shown) at Mach 0.2, Angle of Attack 16°, and Sideslip Angle 0°.

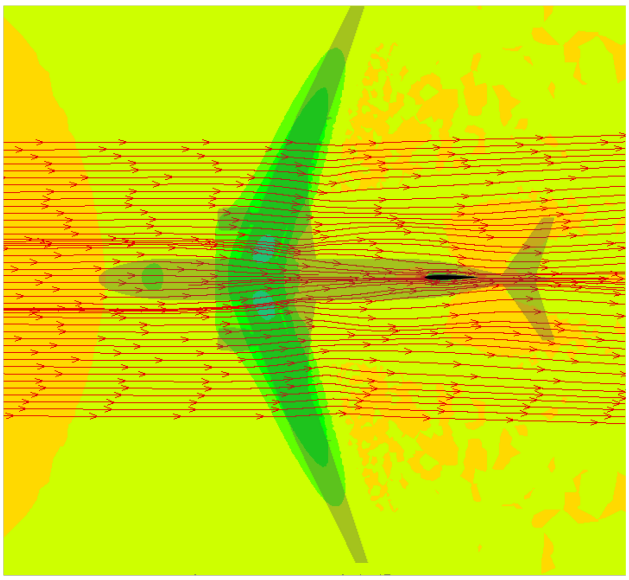

Figure 27 4% Scale TTBW Flow Field in x-y Plane (Notional NACA Airfoil Shown) at Vertical Tail MAC Station at Mach 0.052, Angle of Attack 16°, and Sideslip angle 0°.

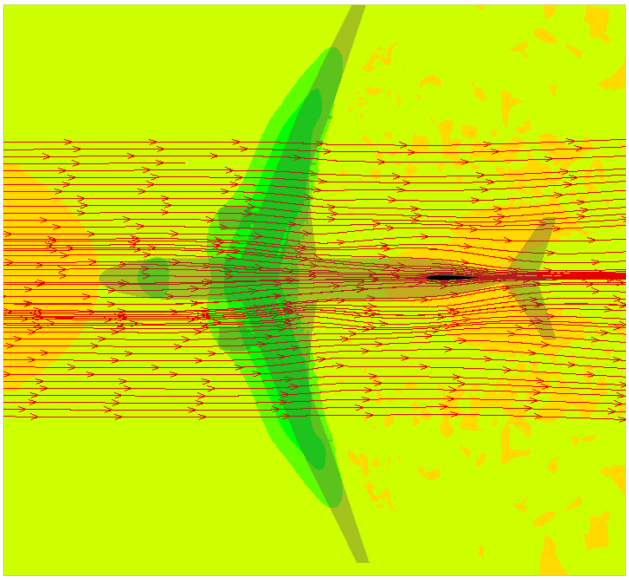

Figure 28 Full Scale TTBW Flow Field in x-y Plane (Notional NACA Airfoil Shown) at Vertical Tail MAC Station at Mach 0.2, Angle of Attack 16°, and Sideslip angle 0°.

Figure 29 shows x-z plane cuts at a high angle of attack of 60° and sideslip angle 0° for the 4% scale model. At this condition, massive flow separation is observed over the wing, strut, and horizontal tail. Figure 31 presents the corresponding x-y plane cut at 60°. A pair of strong vortices form near the wing root leading edge and are convected downstream. These vortices interact with the empennage flow field and induce flow separation, thereby degrading the stability and control effectiveness of the vertical tail. At an angle of attack of 60°, slight flow asymmetry is observed, even with a sideslip angle of 0°. The full scale results at angle of attack of 60° in Fig. 30 and Fig. 32 exhibit the same dominant mechanisms. At this deep-stall condition, Reynolds number effect is diminished: the massive separation

envelops the entire vehicle in both scales. Both scales show large flow separation, slight asymmetric vortex structures, and severe degradation of empennage control effectiveness.

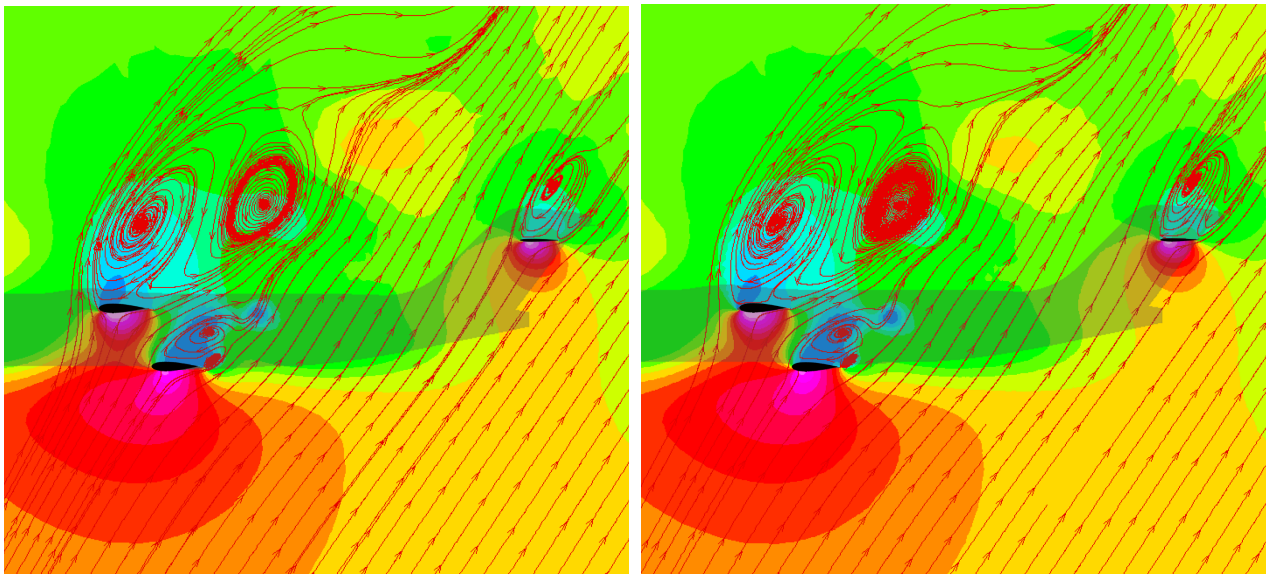

(a) $\eta = -9\%$ (b) $\eta = 9\%$

Figure 29 4% Scale TTBW Flow Field in x-z Plane (Notional NACA Airfoil Shown) at Mach 0.052, Angle of Attack $60°$, and Sideslip Angle $0°$.

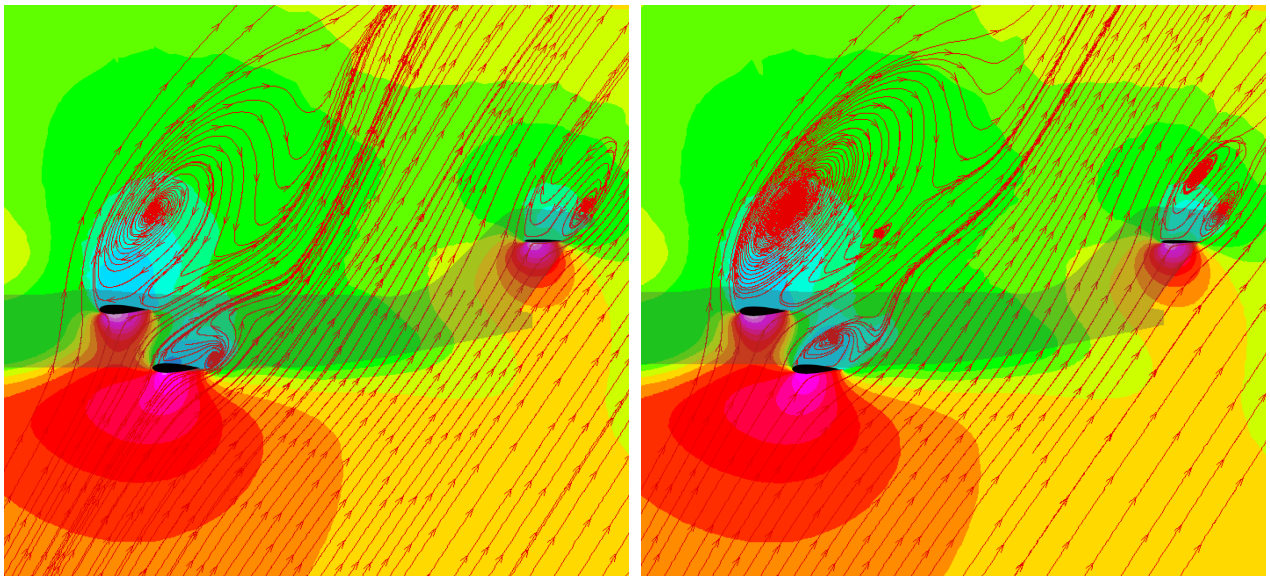

(a) $\eta = -9\%$ (b) $\eta = 9\%$

Figure 30 Full Scale TTBW Flow Field in x-z Plane (Notional NACA Airfoil Shown) at Mach 0.2, Angle of Attack $60°$, and Sideslip Angle $0°$.

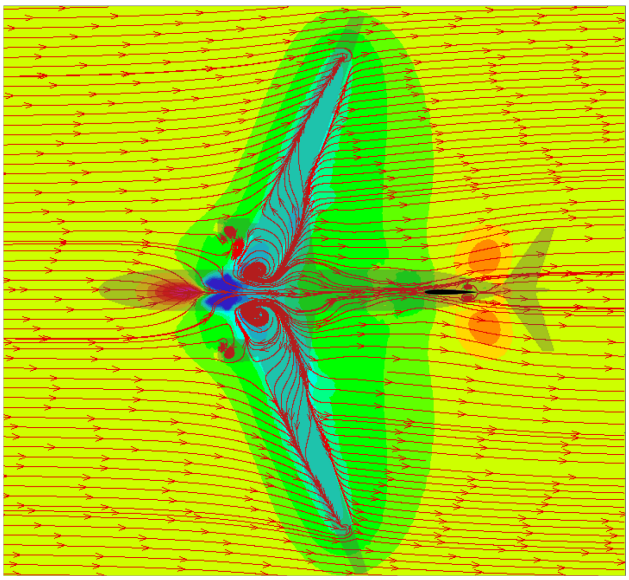

Figure 31 4% Scale TTBW Flow Field in x-y Plane (Notional NACA Airfoil Shown) at Vertical Tail MAC Station at Mach 0.052, Angle of Attack $60°$, and Sideslip Angle $0°$.

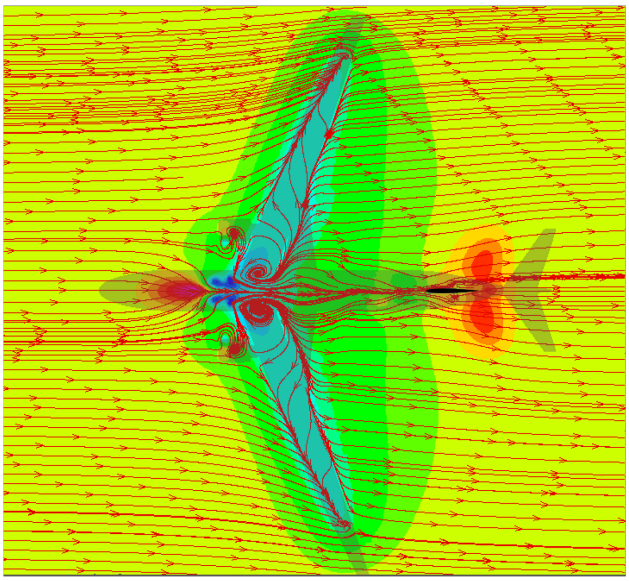

Figure 32 Full Scale TTBW Flow Field in x-y Plane (Notional NACA Airfoil Shown) at Vertical Tail MAC Station at Mach 0.2, Angle of Attack $60°$, and Sideslip Angle $0°$.

Figures 33 - 40 show the same set of x-z and x-y plane cuts for the 4% scale and full scale configurations under a sideslip angle of 15°. Figure 33 displays the x-z cuts at 16° for the 4% scale model, where asymmetry flow is pronounced. Figure 35 presents the x-y plane at 16°, further illustrating lateral asymmetry and unbalanced loading between the two wings. The full scale sideslip results in Fig. 34 and Fig. 36 follow the same trends. The higher Reynolds number again yields slightly more attached flow on the wing surfaces. Nonetheless, the overall flow topology remains consistent between scales.

Figures 37 and 39 show the x-z and x-y plane cuts for the 4% scale, respectively, at 60° angle of attack with a 15° sideslip angle. The extend of flow separation is markedly increased, with severe asymmetry in both pressure and

streamline patterns. Figure 39 show the x-y plane cut at vertical tail MAC station. A negative pressure region develops in front of the wing root leading edge. The vertical tail encounters a highly nonuniform flow field. These effects likely contribute to the loss of directional stability and control effectiveness at high angles of attack. The full scale results at angle of attack of 60° in Fig. 38 and Fig. 40, as with the zero-sideslip condition, Reynold number effect diminishes and shows fully separated flow with strong vortex interactions impinging on the vertical tail.

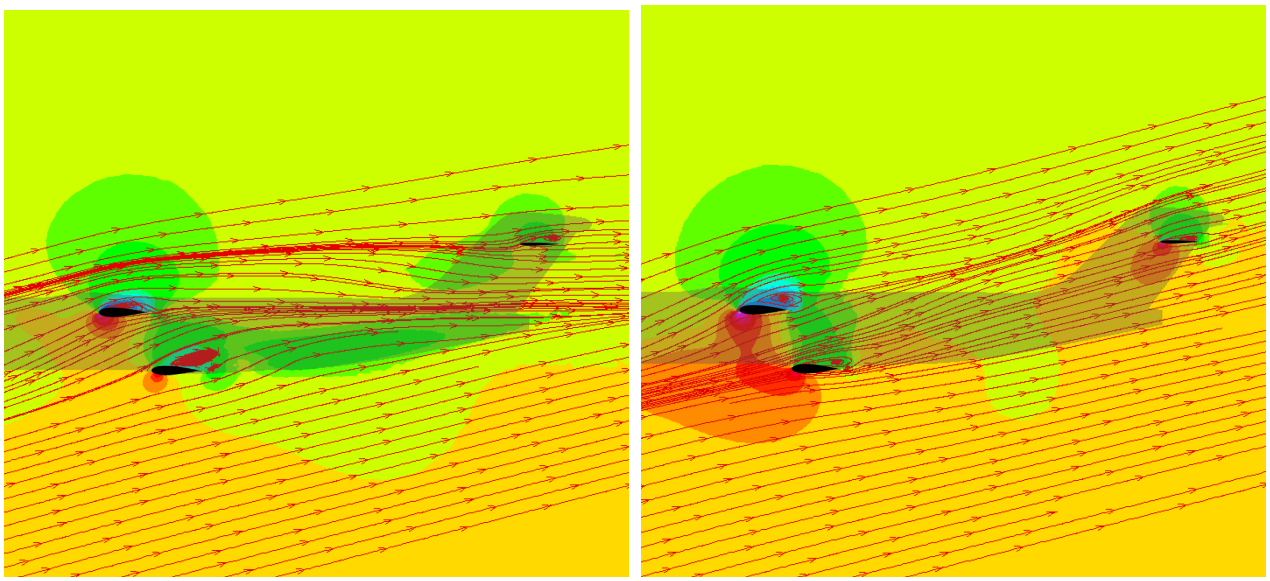

(a) $\eta = -9\%$ (b) $\eta = 9\%$

Figure 33 4% Scale TTBW Flow Field in x-z Plane (Notional NACA Airfoil Shown) at Mach 0.052, Angle of Attack 16°, and Sideslip Angle 15°.

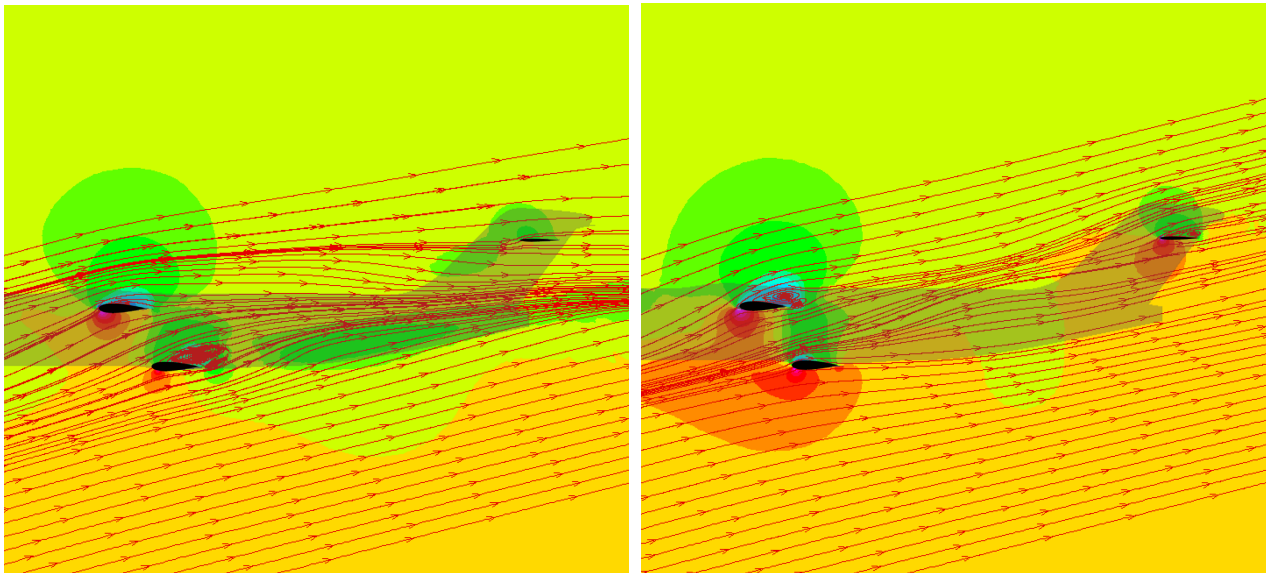

(a) $\eta = -9\%$ (b) $\eta = 9\%$

Figure 34 Full Scale TTBW Flow Field in x-z Plane (Notional NACA Airfoil Shown) at Mach 0.2, Angle of Attack 16°, and Sideslip Angle 15°.

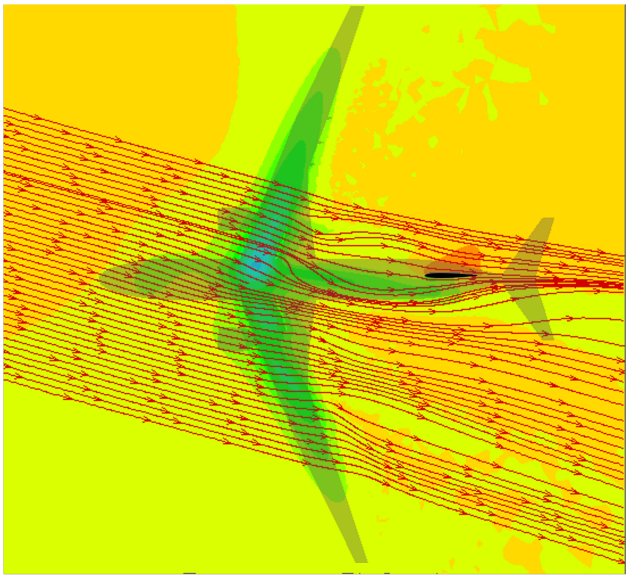

Figure 35 4% Scale TTBW Flow Field in x-y Plane (Notional NACA Airfoil Shown) at Vertical Tail MAC Station at Mach 0.052, Angle of Attack 16°, and Sideslip Angle 15°.

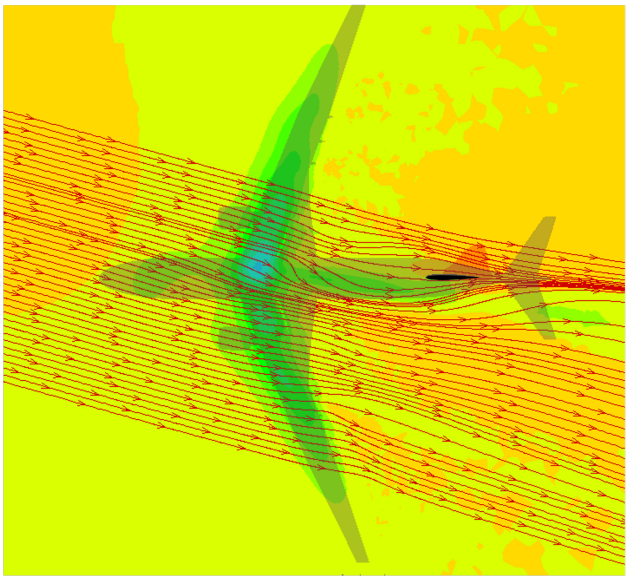

Figure 36 Full Scale TTBW Flow Field in x-y Plane (Notional NACA Airfoil Shown) at Vertical Tail MAC Station at Mach 0.2, Angle of Attack 16°, and Sideslip Angle 15°.

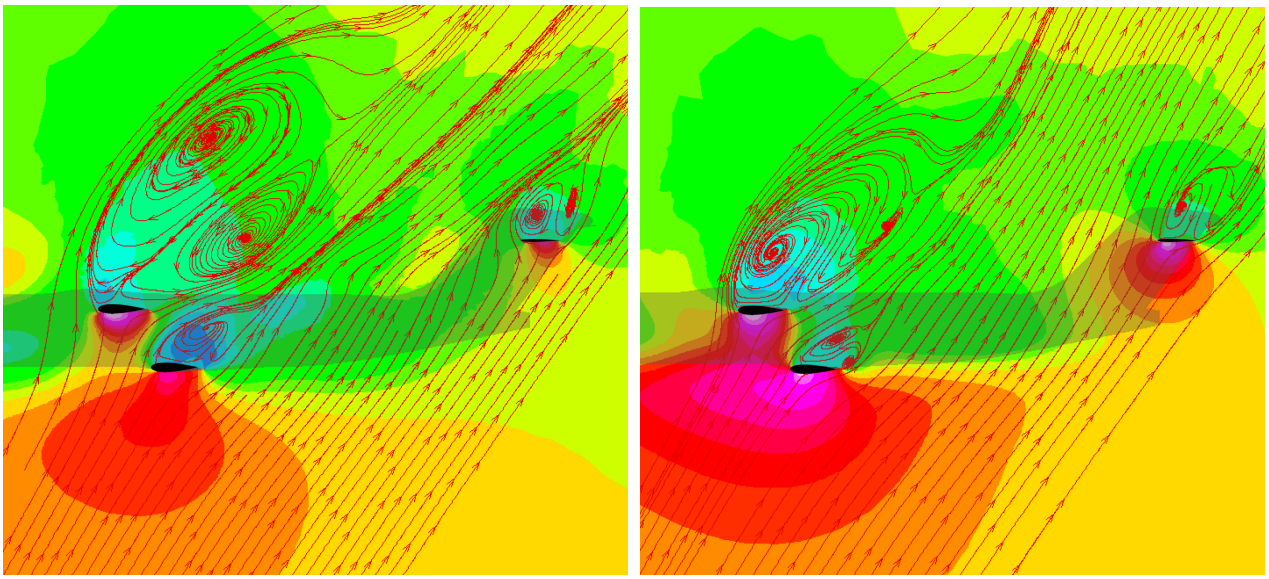

(a) $\eta = -9\%$ (b) $\eta = 9\%$

Figure 37 4% Scale TTBW Flow Field in x-z Plane (Notional NACA Airfoil Shown) at Mach 0.052, Angle of Attack 60°, and Sideslip Angle 15°.

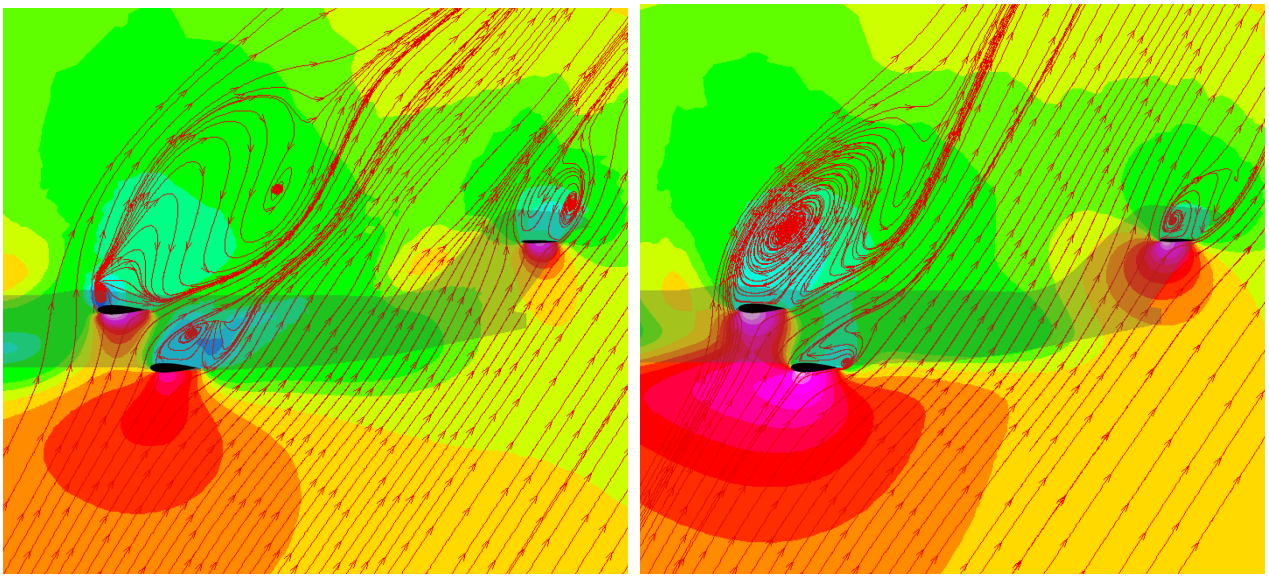

(a) $\eta = -9\%$ (b) $\eta = 9\%$

Figure 38 Full Scale TTBW Flow Field in x-z Plane (Notional NACA Airfoil Shown) at Mach 0.2, Angle of Attack 60°, and Sideslip Angle 15°.

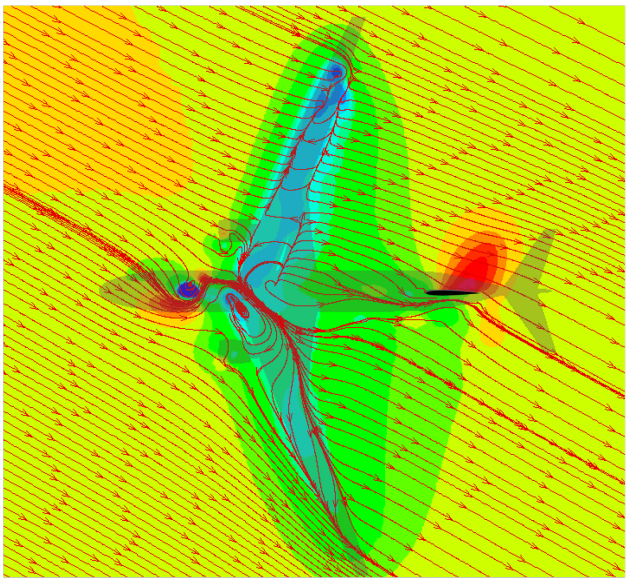

Figure 39 4% Scale TTBW Flow Field in x-y Plane (Notional NACA Airfoil Shown) at Vertical Tail MAC Station at Mach 0.052, Angle of Attack 60°, and Sideslip Angle 15°.

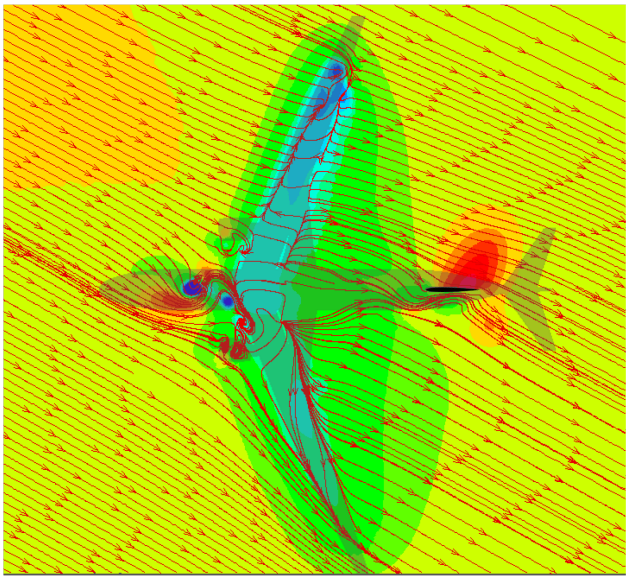

Figure 40 Full Scale TTBW Flow Field in x-y Plane (Notional NACA Airfoil Shown) at Vertical Tail MAC Station at Mach 0.2, Angle of Attack 60°, and Sideslip Angle 15°.

B. Steady State Stability Analysis

Static stability derivatives in both the longitudinal and lateral-directional axes with respect to angle of attack and sideslip angle are obtained by applying perturbations of +/- 0.1° to the angle of attack and sideslip angle, respectively. Figures 41 - 46 present the variations of these stability derivatives across a range of angles of attack from $-10°$ to 60° for both the 4% scale and full scale SUGAR TTBW configurations.

Figure 41 shows the lift coefficient derivative C_{L_α}, which initially increases but drops beyond an angle of attack of 6° for the 4% scale model, reflecting the onset of flow separation and subsequent loss of lift effectiveness. For the full scale configuration, the C_{L_α} drops beyond an angle of attack of 8°. The decline of C_{L_α} indicates nonlinear behaviors in the post-stall conditions.

Figure 42 illustrates the drag coefficient derivative C_{D_α}. For the 4% scale model, C_{D_α} increases monotonically with angle of attack. This trend is consistent with progressive flow separation and associated drag rise. For the full scale model, C_{D_α} reaches maximum at angle of attack 16°, then decreases slightly as the angle of attack increases.

Figure 43 presents the pitching moment coefficient derivative with respective to angle of attack C_{m_α} both the 4% scale and full scale TTBW configurations. For the 4% scale model, the curve displays two pitch breaks occurring around angles of attack of 8° and 16°, corresponding to aerodynamic changes due to wing and horizontal tail surface flow separation, respectively. These features are indicative of nonlinear static longitudinal stability characteristics. For the full scale model, the higher Reynolds number effect delays flow separation, thereby postponing the pitch break to angles of attack of 10° and 16°.

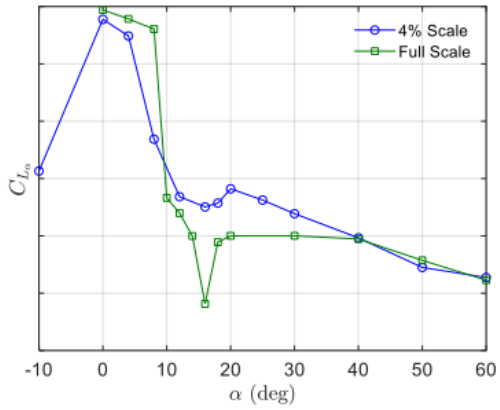

Figure 41 C_{L_α} of TTBW.

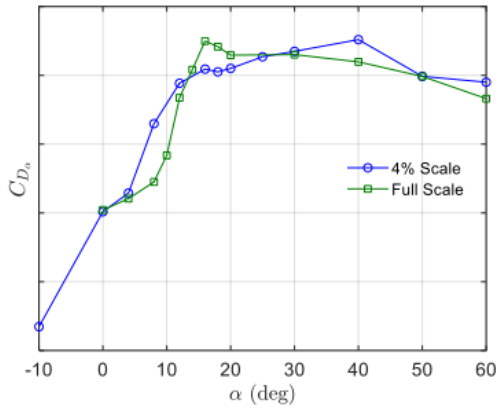

Figure 42 C_{D_α} of TTBW.

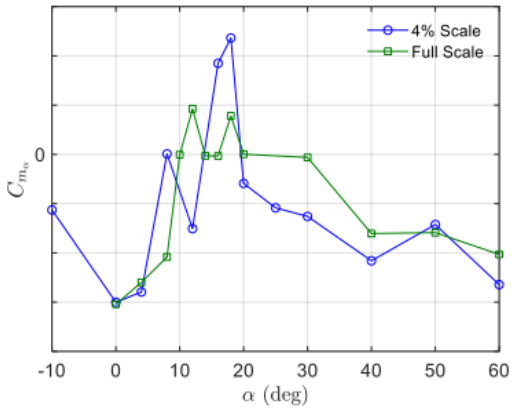

Figure 43 C_{m_α} **of TTBW.**

Figure 44 shows the side force coefficient derivative with respect to sideslip angle, C_{Y_β}, which shows moderate variation but generally trends negatively for both scales.

Figure 45 presents the rolling moment coefficient derivatives with respect to sideslip angle C_{l_β}. This derivative remains stable for angles of attack greater than $-7°$ for the 4% scale model. The rolling moment coefficient derivatives exhibit nonlinearity at higher angles for both scales. But for the full scale configuration, the C_{l_β} becomes more negative between angles of attack of $10°$ to $30°$.

Figure 46 displays the yawing moment coefficient derivatives with respect to sideslip angle C_{n_β}. Notably, C_{n_β} becomes negative at angle of attack $8°$ for the 4% scale model and at angle of attack $11°$ for the full scale model, indicating a loss of static yaw stability, which could lead to yaw divergence behavior. The computed longitudinal and lateral-directional stability derivatives reveal pitch instability at low angle of attack and a narrow yaw stability margin.

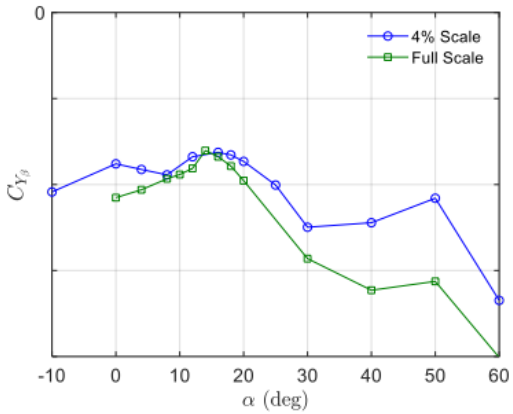

Figure 44 C_{Y_β} **of TTBW.**

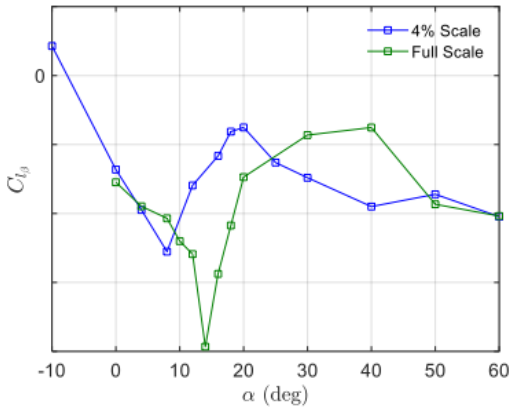

Figure 45 C_{l_β} **of TTBW.**

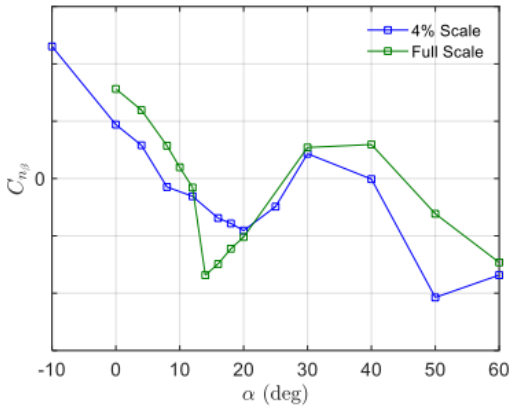

Figure 46 C_{n_β} **of TTBW.**

Conclusions

This paper presents a computational study of a 4% scale wind tunnel model and full scale SUGAR TTBW configuration to investigate its aerodynamic and stability characteristics in deep stall condition. High-fidelity simulations are performed using FUN3D solver to obtain steady-state aerodynamic solutions at low-speed conditions to assess both aerodynamic and stability characteristics at a wide range angle of attack from $-10°$ to $60°$. The comparison between the 4% scale and full scale configurations demonstrates that Reynolds number plays a significant role in determining pre-stall and near-stall aerodynamic behavior. The full scale configuration exhibits higher lift and delayed separation relative to the 4% scale model. The higher Reynolds number effect delays flow separation, thereby improving both the static pitch instability and the static yaw instability margins. These difference diminish at high angles of attack, where fully separated flow dominates and scale effect becomes less important. The sideslip condition produces modest but consistent reduction in lift and shifts in pitching moment, reflecting asymmetric flow interaction between aircraft components. However, the sideslip condition does not fundamentally alter the stall progression or static stability trends for either scale. The SUGAR TTBW model investigated in this study is a research configuration and does not represent any similar configurations under experimental development or in production. Further aerodynamic design modifications currently investigated by Boeing under the SUGAR Phase VI-A contract[5] may potentially lead to a refined SUGAR TTBW configuration with improved static stability characteristics.

Acknowledgment

The authors wish to acknowledge NASA Advanced Air Transport Technology project for the funding support of this work. The authors also acknowledge Boeing Research and Technology and in particular Neal Harrison and Eric Dickey for their research conducted under SUGAR Phase VIb Cooperative Agreement 80NSSC23M0244. The research published in this paper is made possible by the technical data and wind tunnel test data furnished under the contract.

References

[1] Bhatia, M., et. al.. "Structural and Aeroelastic Characteristics of Truss-Braced Wing: A Parametric Study," Journal of Aircraft, Vol 49, No. 1, 2012.

[2] Gundlach, J. F., Tetrault, P. A., Gern, F. H., Nagshineh-Pour, A. H., Ko, A., Schetz, J. A., et. al., "Conceptual Design Studies of a Strut-Braced Wing Transonic Transport," Journal of Aircraft, Vol. 37, No. 6, 2000.

[3] Gur, O., Bhatia, M., Schetz, J.A., Mason, W. H., Kapania, R. K., and Mavris, D. N., "Design Optimization of a Truss-Braced Wing Transonic Transport Aircraft," Journal of Aircraft, Vol. 47, No. 6, 2010.

[4] Harrison, N. A., Beyar, M. D., Dickey, E. D., Hoffman, K., Gatlin, G.M. and Viken, S. A., "Development of an Efficient Mach=0.80 Transonic Truss-Braced Wing Aircraft," AIAA SciTech Conference, AIAA-2020-0011, January 2020.

[5] Harrison, N. A., "SUGAR Phase VI-B Transonic Truss-Braced Wing Enabling Technology Maturation," 2025 UTIAS Workshop on Advanced Technology for Civil Aviation, May 28-30, 2025, Toronto, Canada.

[6] Biedron, R. T., et al., "FUN3D Manual 13.2,", NASA TM-2017-219661, Aug. 2017

[7] Lee-Rausch, E. M., Hammond, D. P., Nielsen, E. J., Pirzadeh, S. Z., and Rumsey, C. L., "Application of the FUN3D Unstructured-Grid Navier-Stokes Solver to the 4th AIAA Drag Prediction Workshop cases," AIAA Aviation Conference, AIAA-2010-4511, January 2019.

[8] Roe, P. L., "Approximate Riemann Solvers, Parameter Vectors and Difference Schemes,", Journal of Computational Physics, Vol. 46, No. 2, 1980, pp. 357-378

[9] Venkatakrishnan, V., "Convergence to Steady State Solutions of the Euler Equations on Unstructured Grids with Limiters,", Journal of Computational Physics, Vol. 118, No. 1, 1995, pp. 120-130

[10] Spalart, P. R. and Allmaras, S. R., "A One-Equation Turbulence Model for Aerodynamic Flows," AIAA Science and Technology Forum and Exposition, AIAA-1992-0439, January 1992.

[11] Biedron, R. T. and Thomas, J. L., "Recent Enhancements To The FUN3D Flow Solver For Moving-Mesh Applications,", AIAA 2009-1360, Jan. 2009

[12] Xiong, J., Nguyen, N., and Bartels, R. E., "Aeroelastic Analysis of Mach 0.8 Transonic Truss-Braced Wing Aircraft ," AIAA Science and Technology Forum and Exposition, AIAA-2022, Jan. 2022.

[13] Harrison, N. A., Sclafani, A. J., Beyar, M. D., Dickey, E. D., and Intravartolo, N. M., "Subsonic Ultra Green Aircraft Research: Phase *IV* Final Report: Vol.2 Transonic Truss-Braced Wing High-Speed Test Report, " NASA/CR-2020-000000, 2020.